J. Fluid Mech. (2003), *vol.* 479, *pp.* 99–124.
DOI: 10.1017/S0022112002003440 Printed in the United Kingdom

Stabilization of a hypersonic boundary layer using an ultrasonically absorptive coating

By A. FEDOROV[1], A. SHIPLYUK[2], A. MASLOV[2], E. BUROV[2] AND N. MALMUTH[3]

[1]Department of Aeromechanics and Flight Engineering, Moscow Institute of Physics and Technology, Zhukovski, 140180, Russia

[2]Institute of Theoretical and Applied Mechanics, Novosibirsk, 630090, Russia

[3]Rockwell Scientific Company, Thousand Oaks, CA 91360, USA

(Received 16 May 2002 and in revised form 12 August 2002)

Experimental and theoretical studies of the effect of an ultrasonically absorptive coating (UAC) on hypersonic boundary-layer stability are described. A thin coating of fibrous absorbent material (felt metal) was selected as a prototype of a practical UAC. Experiments were performed in the Mach 6 wind tunnel on a 7° half-angle sharp cone whose longitudinal half-surface was solid and other half-surface was covered by a porous coating. Hot-wire measurements of 'natural' disturbances and artificially excited wave packets were conducted on both solid and porous surfaces. Stability analysis of the UAC effect on two- and three-dimensional disturbances showed that the porous coating strongly stabilizes the second mode and marginally destabilizes the first mode. These results are in qualitative agreement with the experimental data for natural disturbances. The theoretical predictions are in good quantitative agreement with the stability measurements for artificially excited wave packets associated with the second mode. Stability calculations for the cooled wall case showed the feasibility of achieving a dramatic increase of the laminar run using a thin porous coating of random microstructure.

1. Introduction

For small free-stream disturbances and negligible surface roughness, laminar–turbulent transition is due to amplification of unstable modes in the boundary layer (Malik, Zang & Bushnell 1990; Reshotko 1994). In this case, stability theory and experiment are basic tools for predicting transition loci and developing laminar flow control methods (Mack 1984; Reshotko 1969; Malik 1989). For essentially two-dimensional supersonic and hypersonic flows, the initial phase of transition is associated with excitation and amplification of the first and/or second modes.

The first mode is an extension to high speeds of the Tollmien–Schlichting (TS) waves, which represent viscous instability at low Mach numbers. The inviscid nature of the first mode begins to dominate when the Mach number increases, since compressible boundary-layer profiles contain a generalized inflection point (Mack 1984). This mode may be stabilized by wall cooling, suction and favourable pressure gradient. Another way to damp the first mode is by a very thin perforated sheet stretched over a plenum chamber (Carpenter & Porter 2001). When the TS waves propagate along the boundary layer, the fluctuating pressure forces air in and out of the plenum chamber that modifies the wall boundary conditions for

the disturbances. Carpenter & Porter (2001) conducted a stability analysis for the incompressible boundary layer on a flat plate and showed that the TS waves are stabilized when the wall admittance phase is close to $\frac{1}{2}\pi$. Their analysis is based on linear stability theory for the boundary layer with modified boundary conditions on the perforated wall. Certain aspects of this theoretical modelling are similar to the approach developed by Gaponov (1971, 1975) and Lecoudis (1978) for subsonic boundary layers and by Gaponov (1977) for moderate supersonic flows. Whether the experiments will confirm the theoretical predictions remains to be seen. Carpenter & Porter (2001) indicated several factors that could lead to problems in practice. The theory requires the admittance phase to be very close to $\frac{1}{2}\pi$. This can be achieved only by minimizing the losses through the pores, which leads to severe constraints on the perforated sheet thickness. Another difficulty is associated with pressure variations along the perforated panel. This may lead to areas of quasi-steady inflow and outflow, thereby modifying the mean flow and its stability characteristics.

The second mode results from an inviscid instability driven by a region of supersonic mean flow relative to the disturbance phase velocity. This instability belongs to the family of trapped acoustic modes propagating in a waveguide between the wall and the sonic line (Mack 1984; Guschin & Fedorov 1989). The existence of the second mode was established by the experiments of Kendall (1975), Demetriades (1974), Stetson *et al.* (1983) Stetson & Kimmel (1992*a*, *b*) and Kimmel, Demetriades & Donaldson (1995). Once the second mode sets in, it becomes the dominant instability since its growth rate tends to exceed that of the first mode. For insulated surfaces, this occurs for Mach numbers larger than 4. For cooled surfaces, the second mode can dominate at even lower Mach numbers (Lysenko & Maslov 1984). In contrast to the TS instability, wall cooling destabilizes the second mode. This effect can be important in the transition of hypersonic flows. Since the temperature of a hypersonic vehicle surface is relatively small (less than 0.2 of the adiabatic wall temperature), the TS instability is eliminated by natural cooling, whereas the second mode remains unstable and may trigger early transition. Increasing the laminar run requires the second-mode instability to be diminished.

In high-speed flows, the second mode is associated with disturbances of relatively high frequency corresponding to the ultrasonic band. Malmuth *et al.* (1998) assumed that a passive ultrasonically absorptive coating (UAC) of fine porosity may suppress these fluctuations and, at the same time, may not trip the boundary layer owing to roughness effects, i.e. the passive UAC may stabilize the second and higher modes by a disturbance energy extraction mechanism. This hypothesis was examined by an inviscid linear stability analysis. Using the WKB method, Malmuth *et al.* (1998) formulated the boundary condition on an ultrasonically absorptive wall for the second and higher modes, and showed that the absorption does cause a strong stabilization of the second mode. Later, Fedorov & Malmuth (2001) analysed the absorption effect at finite Reynolds numbers using viscous stability theory and found that viscosity weakly affects the stabilization mechanism. They also considered an ultrasonically absorptive surface of a particular type, namely, a wall covered by a porous coating with cylindrical blind micro-holes, and showed that a relatively thin coating (of thickness ~ 0.1 of the boundary-layer displacement thickness) can dramatically reduce the second-mode growth rate. In contrast to the TS waves (Carpenter & Porter 2001), the second mode is effectively suppressed without a plenum chamber underneath the porous sheet. This significantly simplifies practical application.

These theoretical findings lead to the expectation that a passive porous coating may be exploited for hypersonic laminar flow control. The concept was verified in the

California Institute of Technology GALCIT T-5 shock tunnel (Rasheed *et al.* 2002) by testing a 5° half-angle sharp cone. The cone in these tests had one half of its surface solid and the other a porous sheet that was perforated with equally spaced blind cylindrical holes. The average hole diameter and depth were respectively 60 μm and 500 μm. Average spacing between the holes was 100 μm. The model was instrumented by thermocouples, and the transition onset point was determined from the Stanton number distributions measured simultaneously on both sides of the model for each run. The experiments were performed for the ranges of the free-stream total enthalpy $4.18 \leqslant H_0 \leqslant 13.34\,\mathrm{MJ\,kg^{-1}}$ and the free-stream Mach number $4.59 \leqslant M_\infty \leqslant 6.4$. This study revealed that the porous coating delays transition by a significant amount. For the majority of runs, the boundary layer on the porous surface was laminar up to the model base, whereas transition on the untreated solid surface was observed halfway along the cone. These experiments qualitatively confirmed the theoretical prediction of Fedorov & Malmuth (2001). However, quantitative comparison was not feasible because the cone was not long enough to measure the transition locus on the porous surface. Since the boundary-layer disturbances were not measured, these experiments did not give direct evidence of the second mode instability, and its effect on the transition process was not clear.

A regular microstructure UAC is one possible good starting point for validation of the hypersonic laminar flow control concept. However, most porous materials, which provide efficient absorption of acoustic disturbances, have a random porosity. A practical UAC should be symbiotic with thermal protection systems (TPS) of actual hypersonic vehicles. Since the majority of TPS materials have random microstructures, a randomly porous coating is of most interest for applications. This motivated the theoretical and experimental studies of a randomly porous UAC to be discussed herein. The investigation is focused on direct measurements of the boundary-layer disturbances and verification of the stability theory predictions.

2. Experimental apparatus

2.1. *Wind tunnel*

The experiments were conducted in the T-326 hypersonic blow-down wind tunnel with open-jet test section (Grigoriev *et al.* 1972) at the Institute of Theoretical and Applied Mechanics (ITAM) of the Siberian Branch of Russian Academy of Sciences in Novosibirsk. The diameter of the axisymmetric contoured nozzle of this facility is 200 mm. Run-time can be as long as 30 min, subject to a Mach number flow-field non-uniformity of 0.7% in the flow core at a freestream Mach number $M_\infty \approx 6$. The test core diameter is approximately 180 mm. Typical of conventional hypersonic wind tunnels, the noise level is about 1%. During the experiment, pressure, P_0, and temperature, T_0, in the settling chamber are kept constant, with accuracies of 0.06% and 0.25%, respectively.

2.2. *UAC parameters*

Characteristics of a porous coating must meet certain requirements to suppress the boundary-layer instability effectively. For the wind tunnel tests, the boundary-layer thickness on a 7° half-angle cone is approximately 1 mm (see §4.1 and figure 8). According to the experimental observations of Kendall (1975), Demetriades (1974), Stetson *et al.* (1983), Stetson & Kimmell (1992*a*, *b*) and Kimmel *et al.* (1995), the second-mode wavelength is approximately twice the boundary-layer thickness, i.e. it is ~ 2 mm in the case considered. The characteristic size of the porous coating should

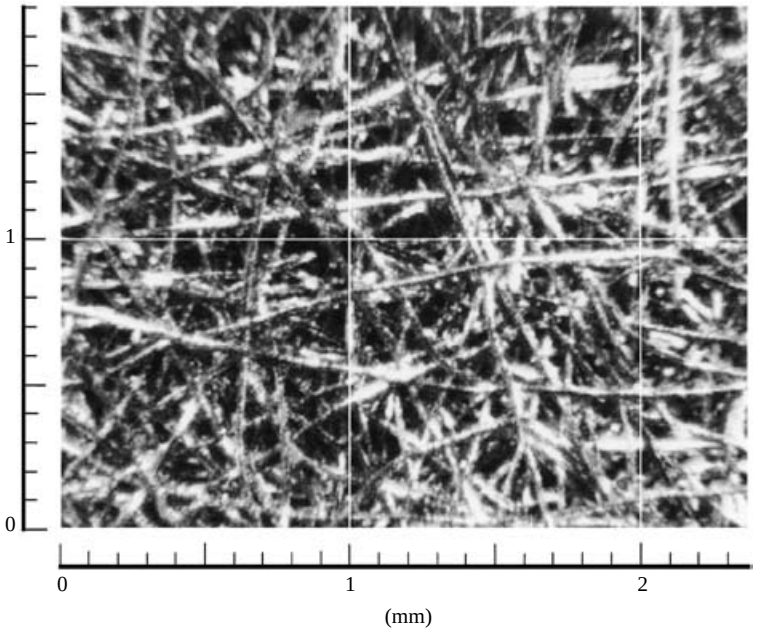

FIGURE 1. Magnified sixty-fold image of the upper surface of the felt-metal coating; $1 \times 1\,\mathrm{mm}^2$ grid.

be much smaller than the disturbance wavelength to avoid resonant interactions with the porous-layer microstructure and minimize roughness effects. On the other hand, the pore size should be large enough to diminish the rarefied gas effect and provide intensive absorption of the boundary-layer disturbances in the frequency band 200–400 kHz associated with the second mode. Compromising these constraints we chose the felt-metal coating, which is composed of stainless steel fibres of diameter $d = 30\,\mu\mathrm{m}$. To provide integrity of the coating, the fibres were hard sintered randomly on a solid stainless steel sheet of thickness 0.245 mm. Then, they were rolled to a porosity of 75%. The porous layer has a thickness of 0.75 mm resulting in a total thickness of the felt metal sheet of 1 ± 0.1 mm. Magnified images of the porous surface (one of them is shown in figure 1) reveal that the average pore size is $\approx 100\,\mu\mathrm{m}$. This results in 20 pores per boundary-layer disturbance wavelength.

2.3. *Model*

The model was a 7° half-angle sharp cone of 500 mm length (see figure 2) consisting of three parts: (i) a sharp cone 65 mm in length and 0.1 mm nose radius; (ii) a middle part 65 mm in length containing an electric glow discharge perturber; and (iii) a base portion 370 mm in length. Half of the base part is covered by a felt-metal sheet as shown in figure 2. Roughness of the solid surface is 0.6 μm. The model is equipped with a three-dimensional perturber providing a high-frequency glow discharge in a small chamber. Artificial disturbances generated by the perturber are introduced into the boundary layer through an orifice of 0.4 mm diameter located at a distance of 69 mm from the model nose. The perturber construction is similar to that used for excitation of artificial wave packets in supersonic boundary layers (Kosinov, Maslov & Shevelkov 1990). Maslov *et al.* (2001) have successfully applied this technique to hypersonic flows.

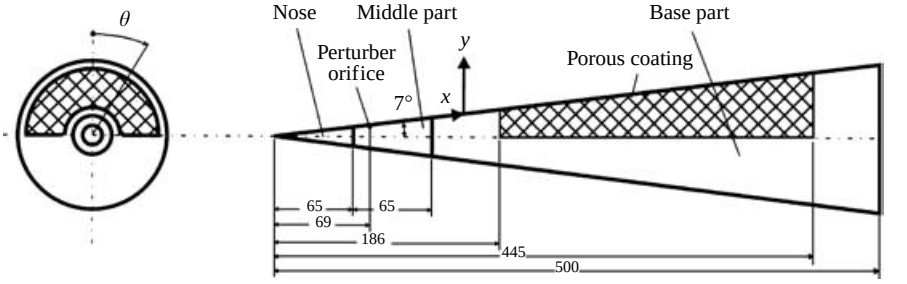

FIGURE 2. Schematics of the model; dimensions are in mm.

A major challenge in the construction of the model was attachment of the felt-metal sheet to the basic cone. After bending, the porous layer expanded, leading to its thickening by approximately 20%. This complicated the determination of the undercut of the basic cone to allow flash attachment of the felt-metal sheet. To minimize mismatch between the porous and solid surfaces, the felt-metal sheet was attached to the base cone and then ground until the surface irregularity was reduced to 0.05 mm.

Another difficulty was detachment of the felt-metal filaments because of sheet stretching. Examination of the porous surface under a microscope showed that some of the detached filaments protrude from the surface approximately 3–4 mm. These filaments (about 1500–2000) were manually trimmed off.

The model was installed at zero angle of attack. The estimated misalignment between the cone axis and the free-stream direction was less than 0.05°. This allows three-dimensional distortions of the mean flow to be neglected.

2.4. *The measuring system*

To determine the free-stream parameters, IPD-89008 pressure gauges and k-type thermocouples measured pressures and temperatures in the settling chamber and provided accuracies of 0.15% and 0.1%, respectively. The free-stream Mach number was determined using Pitot measurements.

Two traverse gears were used in the experiment. A three-component traverse system provided X, Y, Z displacements of the hot-wire probe to an accuracy of 0.01 mm. A special unit was used to roll the whole cone around its X-axis and measure transverse distributions of wave packets. The roll angle, Θ, was controlled within an accuracy 0.1°.

The high-frequency glow discharge system consisted of clock and high-voltage generators. The clock generator signal was used to trigger the high-voltage generator and synchronize hot-wire measurements with the high-voltage generator initiation. The high-voltage generator produced voltage pulses up to 2000 V, of 1 μs duration and pulse frequency up to 400 kHz. During the run, the glow discharge was controlled visually through optical windows and a mirror in the test section.

A constant-current hot-wire anemometer, custom built at ITAM, was used to measure mass flow fluctuations. The hot-wire probes were made of tungsten wire of 5 μm diameter and 1 mm length which was welded to pointed stings. The overheat ratio was 0.5 and the frequency response of the hot-wire anemometer was 500 kHz. The constant and alternating components of the hot-wire signal were measured by a 12-bit analogue-digital converter with a sampling frequency of 5 MHz. At each measurement station, 98 time-series of 4096 samples were acquired. An analogue

Surface	P_0 (MPa)	T_0 (K)	M_∞	M_e	$Re_{1\infty}$ (m^{-1})	Re_{1e} (m^{-1})	T_w/T_0	f (kHz)
Solid	1.0 ± 0.002	395 ± 3	5.92	5.3	11.8×10^6	15.4×10^6	0.79–0.83	280
Porous	1.0 ± 0.002	391 ± 1	5.92	5.3	12.0×10^6	15.6×10^6	0.81–0.84	280

TABLE 1. Basic parameters.

signal of the main generator initiating glow discharge was used to trigger ADC. Details of the processing techniques have been discussed by Maslov *et al.* (2001).

2.5. *Processing of the disturbance characteristics*

To obtain the amplitude, A, and phase, Φ, of artificially excited disturbances, the discrete Fourier transform is used

$$A(X, Y, \Theta)\exp(\mathrm{i}\Phi(X, Y, \Theta)) = \frac{2}{N}\sum_{j=1}^{N}\rho U_n(X, Y, \Theta, t_j)\exp(-2\mathrm{i}\pi f t_j),$$

where N is the sample count in the time-series, f is the disturbance frequency, and $\rho U_n(X, Y, \Theta, t_j)$ is the time-series of mass flow pulsations. The artificial wave packet is represented as a decomposition of elementary waves. For this purpose the transverse wave spectra are calculated as

$$SA(x, \beta)\exp(\mathrm{i}SF(x, \beta)) = \int_{-\Theta_0}^{\Theta_0} A(x, \Theta)\exp(\mathrm{i}\Phi(x, \Theta))\exp(-i\beta\Theta)\mathrm{d}\Theta,$$

where SA and SF are the amplitude and phase spectra with respect to the transverse wave number β.

3. Measurement results

Basic experimental parameters are given in table 1, where Re_1 is the unit Reynolds number, T_w is the wall temperature, f is the frequency of artificial disturbances, and the subscript e denotes quantities at the upper boundary-layer edge. Hypersonic viscous–inviscid interaction is neglected, since the interaction parameter $\chi = M_e^3/\sqrt{Re_X}$ (Hayes & Probstein 1959) is less than 0.1 for the region $X > 94$ mm, where all measurements are conducted.

Figures 3(a) and 3(b) show the mean flow velocity U/U_e and the r.m.s. mass flow pulsations versus the vertical coordinate, Y, normalized with respect to the boundary-layer thickness δ ($U(\delta) = 0.99U_e$). Symbols correspond to the hot-wire measurements on the (i) porous and (ii) solid surfaces at $X = 224.9$ mm; the solid line (iii) in figure 3(a) shows the self-similar solution of the laminar boundary-layer equations discussed in § 4.1. The good agreement between the theoretical and experimental mean flow profiles indicates that the boundary layers on both surfaces are laminar. Similar results were obtained at the cross-sections where hot-wire measurements were made. Note that the disturbance profiles for both surfaces have maxima located at $Y/\delta = 0.8$ (see figure 3b).

Mass flow disturbance spectra were measured at the normal coordinate Y corresponding to the disturbance maxima. Hot-wire measurements were conducted at the equally spaced X-stations given in table 2. The first station S1 was chosen near the leading edge of the porous surface ($X = 185$ mm). Disturbance spectra are

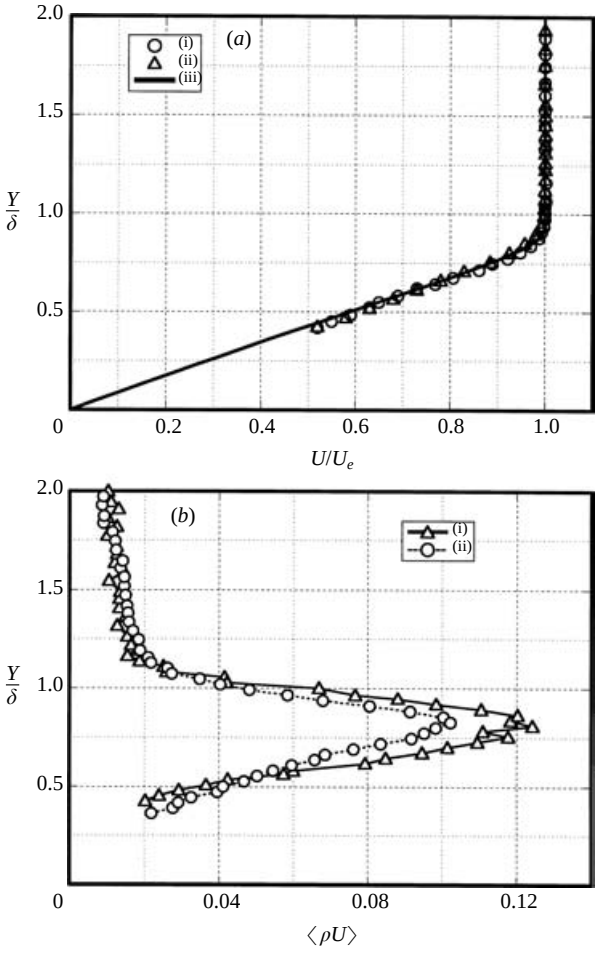

FIGURE 3. Comparison profiles of (*a*) mean velocity and (*b*) r.m.s. mass-flow pulsations for (i) porous and (ii) solid surfaces; (iii) self-similar profile.

Surface	S1	S2	S3	S4	S5
Solid	192.8	217.8	242.9	268.0	293.0
Porous	189.1	214.2	239.2	264.3	289.4

TABLE 2. Locations of the measurement stations (X mm).

shown in figures 4(*a*) and 4(*b*) for the solid and porous surfaces, respectively. At the upstream station S1, the spectra are similar on both surfaces. Downstream from S1, the spectrum evolutions are quite different. On the solid surface the disturbance spectra look very similar to those measured by Stetson & Kimmel (1992*b*) on a sharp cone at $M_\infty = 8$; they correspond to the second mode instability. At the upstream station S1, the second mode is observed at the frequency $f \approx 340$ kHz. Downstream from S1, its amplitude quickly increases, whereas its central frequency decreases to 275 kHz at the last station S5. On the porous surface, the low-frequency disturbances

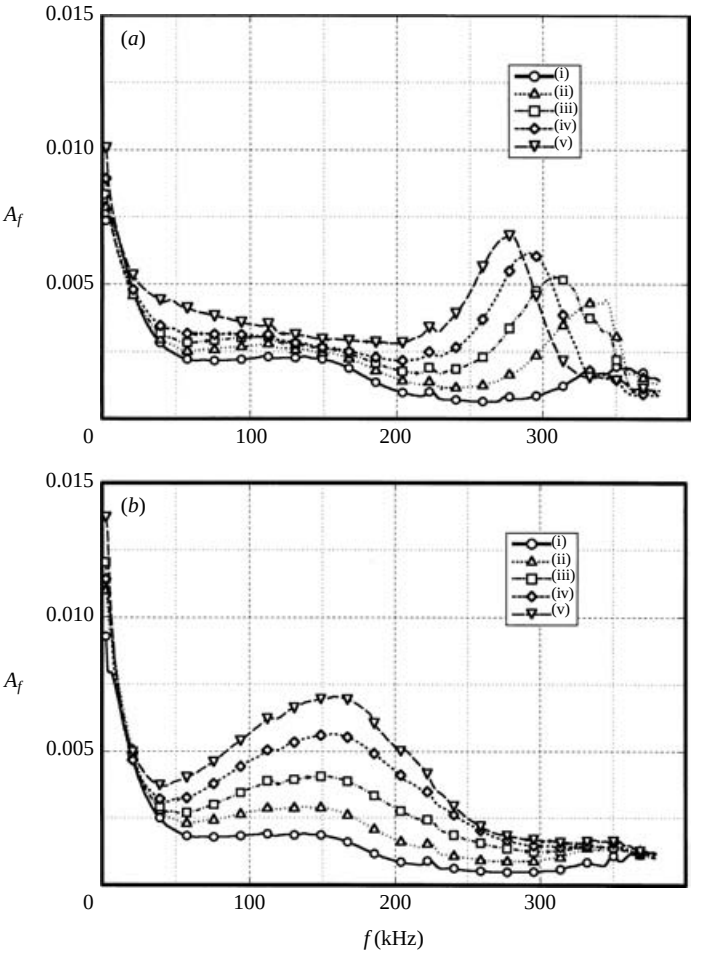

FIGURE 4. Disturbance spectra for (*a*) solid and (*b*) porous surfaces; curves (i)–(v) correspond to stations S1–S5 of table 2.

associated with the first mode are destabilized in the frequency band 100–200 kHz. At the upstream station S1, a small increase of the disturbance spectrum is noticeable near the frequency 350 kHz that may be relevant to the second mode. However, there is no evidence of the second mode at stations S2–S5. These data demonstrate that the porous coating strongly stabilizes the second mode and destabilizes the first mode under natural flow conditions.

To investigate the second-mode stabilization effect a series of experiments was conducted with artificially excited wave packets. The artificial disturbances were generated at a frequency of 280 kHz, which corresponds to the maximum of the second-mode amplitude observed on the solid surface at station S5 for natural disturbances (see the spectrum (v) in figure 4*a*). At first, the artifical wave packet was measured on the solid surface. Then, the middle part with the perturber was rolled 180°, and experiments were carried out on the porous surface. This approach allows for excitation of the wave packets with almost identical initial amplitudes on both surfaces. The disturbance characteristics were measured at the same stations as for natural disturbances (see table 2).

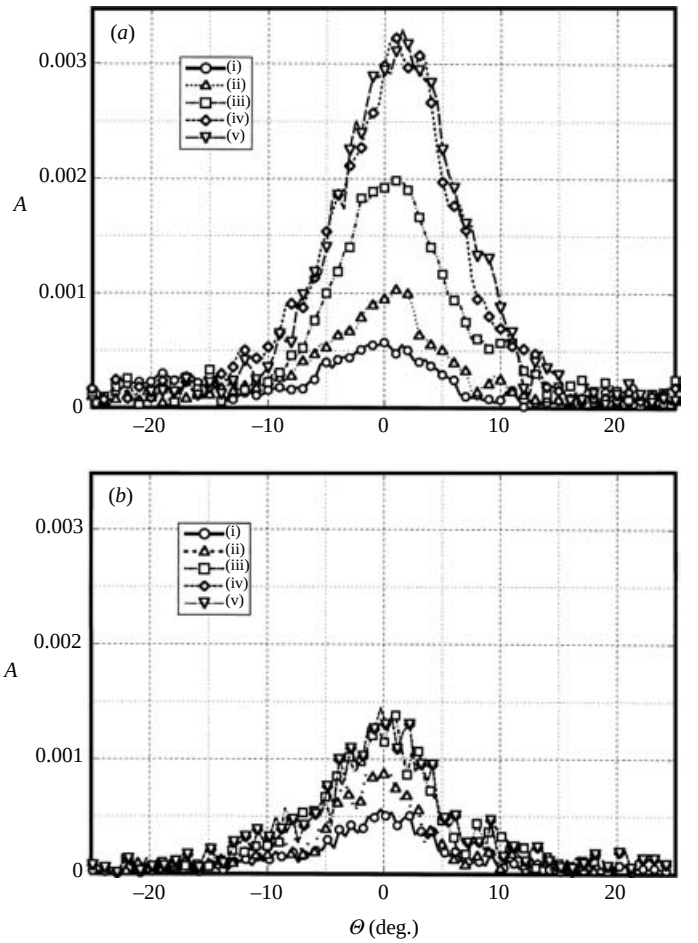

FIGURE 5. Transverse distributions of amplitude of artificial wave packet for (*a*) solid and (*b*) porous surfaces; curves (i)–(v) correspond to stations S1–S5 of table 2.

The disturbance phase measured at the wave packet centre is a linear function of X in the range $X = 240$–300 mm. For the solid and porous surfaces, the phase velocities are equal to $(0.896 \pm 0.03)U_e$, which is consistent with the value $0.916U_e$ calculated for the second mode using the theoretical model of § 4.

Transverse distributions of the wave packet amplitude are shown in figures 5(*a*) and 5(*b*) for the solid and porous surfaces, respectively. These distributions have a single peak in the middle of the wave packet (at $\Theta \approx 0$) for all X-stations. The porous coating reduces the disturbance amplitude more than twice. The transverse wave spectra (the β-spectra resulting from the Fourier transform of the transverse distributions) are shown in figures 6(*a*) and 6(*b*). These spectra have a single peak at $\beta = 0$ for all X-stations, i.e. two-dimensional waves are dominant. This is typical for the second mode. On the porous surface, the maximum amplitude is essentially smaller than on the solid surface, clearly demonstrating boundary-layer stabilization.

Longitudinal distributions of the mass flow disturbance amplitude SA_0 at $\beta = 0$ are shown in figure 7 for the solid (i) and porous (ii) surfaces. The amplitudes of natural disturbances with a frequency $f = 280$ kHz are also shown for comparison. They were normalized to match the distributions at the initial X-station. On the solid surface,

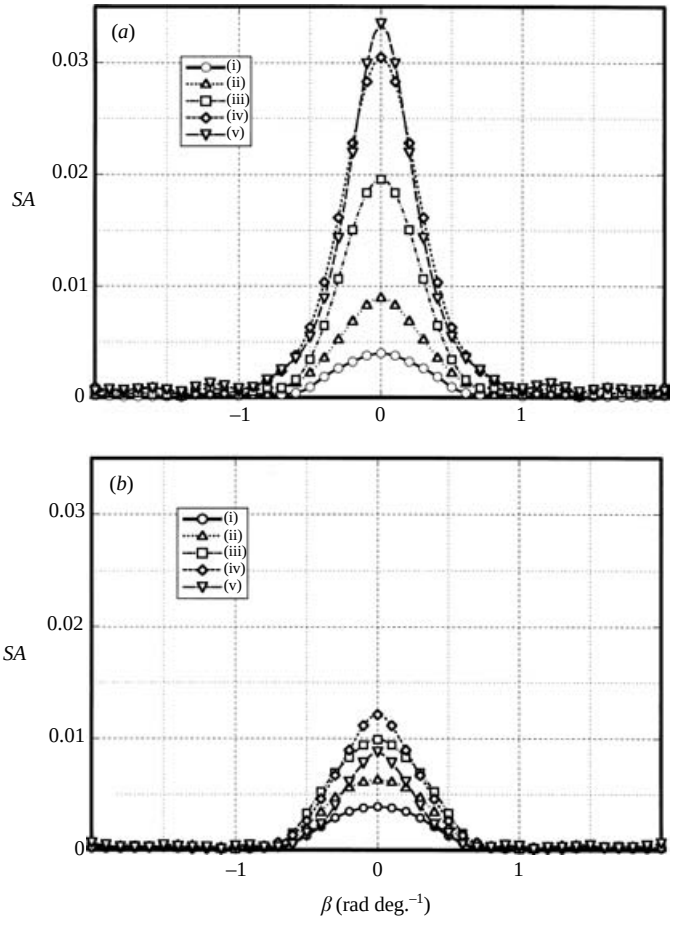

FIGURE 6. β-spectra for (a) solid and (b) porous surfaces; curves (i)–(v) correspond to stations S1–S5 of table 2.

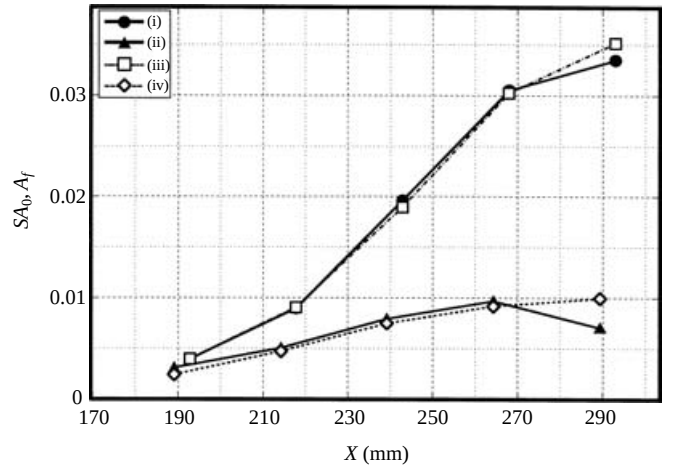

FIGURE 7. Longitudinal distribution of mass flux pulsations amplitude for solid ((i) artificial and (iii) natural disturbances) and porous ((ii) artificial and (iv) natural disturbances) surfaces.

the disturbance amplitude exponentially grows up to $X = 243$ mm. Downstream of this location, the amplification rate decreases. On the porous surface, the amplitude increases approximately twice as slowly as on the solid surface. Moreover, disturbance decay begins downstream of the station $X = 264$ mm. The amplitude distributions of artificial and natural disturbances are very close to each other. This indicates that two-dimensional waves are dominant in the natural disturbance field in the same manner as for artificial wave packets.

4. Stability analysis

4.1. *Mean flow*

For the laminar boundary layer on a flat plate or a sharp cone at zero angle of attack, the boundary-layer equations are written in the self-similar form (Hayes & Probstein 1959)

$$(Cf'')' + ff'' = 0, \tag{4.1}$$

$$\left(\frac{C}{\mathrm{Pr}}g'\right)' + fg' + \frac{U_e^{*2}}{H_e^*}\left[C\left(1 - \frac{1}{\mathrm{Pr}}\right)f'f''\right]' = 0, \tag{4.2}$$

$$C = \frac{\rho^*\mu^*}{\rho_e^*\mu_e^*}, \frac{U_e^{*2}}{H_e^*} = \frac{(\gamma-1)M_e^2}{1+\frac{1}{2}(\gamma-1)M_e^2}, \frac{\rho_e^*}{\rho^*} = \left(1+\tfrac{1}{2}(\gamma-1)M_e^2\right)g - \tfrac{1}{2}(\gamma-1)M_e^2 f'^2. \tag{4.3}$$

Hereinafter, $f'(\eta) = U^*/U_e^*$, $g(\eta) = H^*/H_e^*$, ρ, μ, Pr and γ denote the streamwise velocity, total enthalpy, density, viscosity, Prandtl number and specific heat ratio, respectively; primes denote differentiation with respect to η, and asterisks denote dimensional quantities. The independent variables are given by the Howarth–Dorodnitsyn transformations and Mangler transformation by the coordinates

$$\xi = \int_0^{x^*} \rho_e^*\mu_e^*U_e^*r_w^{*2j}\,\mathrm{d}x^*, \quad \eta = \frac{U_e^*r_w^{*j}}{\sqrt{2\xi}}\int_0^{y^*}\rho^*\,\mathrm{d}y^*, \tag{4.4}$$

where x is along an external streamline, y is normal to the body surface, r_w is the distance from the symmetry axis to the wall surface; $j = 0$ for two-dimensional flow and $j = 1$ for axisymmetric flow. The porous coating is assumed to affect the mean flow only weakly. Accordingly, the conventional no-slip boundary conditions are imposed on the wall surface

$$\eta = 0: \quad f = f' = 0, \quad g = g_w \quad (\text{or } g' = 0 \text{ for adiabatic wall}), \tag{4.5}$$

$$\eta \to \infty: \quad f' = 1, \quad g = 1. \tag{4.6}$$

In all calculations discussed hereinafter, the fluid is a perfect gas of $\gamma = 1.4$ and $Pr = 0.708$. The viscosity temperature dependency is approximated by Sutherland's law

$$\mu(T) = \frac{(1+S)}{(T+S)}T^{3/2}, \tag{4.7}$$

where $S = 110/T_e^*$, $\mu = \mu^*/\mu_e^*$ and $T = T^*/T_e^*$ are non-dimensional viscosity and temperature. The mean-flow parameters correspond to the experimental conditions discussed in §3: $M_e = 5.3$; $T_e^* = 59.3$ K; the local unit Reynolds number $Re_{1e} = U_e^*/\nu_e^* = 15.5 \times 10^6\,\mathrm{m}^{-1}$; the wall temperature, $T_w^* = 5.5\,T_e^*$, is close to the adiabatic wall temperature.

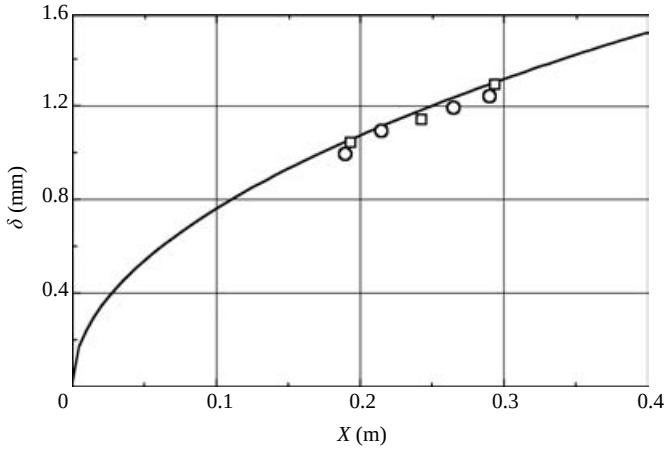

FIGURE 8. Boundary-layer thickness at $Re_1 = 15.5 \times 10^6\,\mathrm{m}^{-1}$, $M_e = 5.3$, $T_e = 59.3\,\mathrm{K}$, and the wall temperature $T_w = 5.5\,T_e$. —, theory; ○, experiment, porous surface; □, experiment, solid surface.

Figure 8 shows that the theoretical boundary-layer thickness δ correlates well with the experimental data for the solid and porous surfaces of the cone. Since wall temperature, $T_w^* \approx 326\,\mathrm{K}$, is close to room temperature, thermal deformations of the porous coating during the wind-tunnel run are neglected.

4.2. *Linear stability problem*

The stability analysis herein includes the non-parallel effect associated with downstream growth of the boundary-layer thickness. Cone surface curvature and conical divergence of streamlines are neglected in this model. It is based on the method developed by Gaster (1974) for incompressible boundary layers and extended by Padhye & Nayfeh (1979) to compressible flows. This method (with insignificant variations) has been used to investigate the non-parallel effect on stability of supersonic boundary layers (Gaponov 1980; El-Hady 1980; Tumin & Fedorov 1982). Its extension to the case of multiple modes was discussed in Zhigulev & Tumin (1982) and Fedorov & Khokhlov (2002).

Following Fedorov & Khokhlov (2002), we outline the non-parallel stability analysis for a monochromatic wave. The coordinates (x, y, z) are made non-dimensional using the boundary-layer scale $l^* = \sqrt{\nu_e^* L^*/U_e^*}$, where the distance L^* from the leading edge is assumed to be much larger than l^*, and the ratio $\varepsilon = l^*/L^*$ is treated as a small parameter. Time t and pressure P are referenced to l^*/U_e^* and $\rho_e^* U_e^{*2}$, respectively; other flow characteristics are non-dimensionized by normalizing them to upper boundary-layer edge quantities. Introducing the slow variable, $x_1 = x^*/L^* = \varepsilon x$, we specify the mean-flow velocity components (U, V) and temperature T as

$$U = U(x_1, y), \quad V = \varepsilon V_0(x_1, y), \quad T = T(x_1, y). \tag{4.8}$$

A monochromatic disturbance is represented by the vector function

$$\begin{gathered} \boldsymbol{Z} = \left(u, \frac{\partial u}{\partial y}, v, p, \theta, \frac{\partial \theta}{\partial y}, w, \frac{\partial w}{\partial y}\right)^T, \\ \boldsymbol{Z}(x, y, z, t) = \boldsymbol{F}(x, y) \exp(\mathrm{i}\,\beta z - \mathrm{i}\,\omega t), \end{gathered} \tag{4.9}$$

where u, v, w, p and θ are velocity components, pressure and temperature; $\beta = \beta^* l^*$ and $\omega = \omega^* l^*/U_e^*$. The amplitude vector-function $\boldsymbol{F}(x, y)$ satisfies a system of partial differential equations that result from a Fourier transform of the linearized Navier–Stokes equations with respect to time and the z-coordinate. These equations with the boundary conditions can be written in the matrix-operator form

$$\mathbf{H}(y, \partial_y, x_1, \varepsilon\partial_{x_1}, \omega, \beta)\boldsymbol{F} = 0. \tag{4.10}$$

$$y = 0: \quad F_1 = A_x F_4, \quad F_3 = A_y F_4, \quad F_5 = A_\theta F_4, \quad F_7 = A_z F_4, \tag{4.11}$$

$$y \to \infty: \quad F_1, F_3, F_5, F_7 \to 0. \tag{4.12}$$

Here admittances A_x, A_y, A_z and thermal admittance A_θ are complex quantities, which couple velocity and temperature disturbances with the pressure perturbations on the porous surface. They depend on properties of the porous material, mean flow characteristics on the wall surface, and disturbance frequency. These dependencies will be specified in §4.3. For the solid wall $A_x = A_y = A_z = A_\theta = 0$, which corresponds to no-slip conditions and zero temperature perturbation on a surface of high thermal conductivity.

We consider a partial solution of the problem (4.10)–(4.12), which is a discrete mode of the complex eigenvalue $\alpha(x_1, \beta, \omega)$. The amplitude vector-function is expressed as

$$\boldsymbol{F} = (\boldsymbol{F}_0 + \varepsilon\boldsymbol{F}_1 + \ldots)\exp(\mathrm{i}\,\varepsilon^{-1}S), \quad S = \int \alpha(x_1)\mathrm{d}x_1 \tag{4.13}$$

Substituting (4.13) into (4.10)–(4.12) and grouping terms of the same order of magnitude with respect to ε we obtain a sequence of problems for $\boldsymbol{F}_j(x_1, y)$, $j = 0, 1, \ldots$. In the zeroth-order approximation, the eigenvalue problem for a locally parallel mean flow is written as

$$\left(\frac{\partial}{\partial y} - \boldsymbol{H}_0\right)\boldsymbol{F}_0 = 0, \tag{4.14}$$

$$y = 0: \quad F_{01} = A_x F_{04}, \quad F_{03} = A_y F_{04}, \quad F_{05} = A_\theta F_{04}, \quad F_{07} = A_z F_{04}, \tag{4.15}$$

$$y \to \infty: \quad F_{01}, F_{03}, F_{05}, F_{07} \to 0. \tag{4.16}$$

Here, the matrix $\boldsymbol{H}_0$ has dimension 8×8; its non-zero elements are given in the Appendix. Solution of the problem (4.14)–(4.16) is expressed as

$$\boldsymbol{F}_0 = c(x_1)\boldsymbol{\zeta}(x_1, y, \alpha), \tag{4.17}$$

where ζ is the eigenvector normalized by a certain condition, such as the pressure disturbance amplitude on the wall surface is $\zeta_4(x_1, 0, \alpha) = 1$. For spatial instability of two-dimensional boundary layers, the frequency ω and the transverse wavenumber component β are real, whereas α is a complex eigenvalue. If $\mathrm{Im}\,\alpha < 0$, then the disturbance amplifies downstream with the spatial growth rate $\sigma_\alpha = -\mathrm{Im}\,\alpha$. The amplitude coefficient $c(x_1)$ is determined from the first-order approximation, which leads to the inhomogeneous problem

$$\left(\frac{\partial}{\partial y} - \boldsymbol{H}_0\right)\boldsymbol{F}_1 = -\mathrm{i}\frac{\partial \boldsymbol{H}_0}{\partial \alpha}\frac{\partial \boldsymbol{F}_0}{\partial x_1} + \boldsymbol{H}_1\boldsymbol{F}_0, \tag{4.18}$$

$$y = 0: \quad F_{01} = A_x F_{04}, \quad F_{03} = A_y F_{04}, \quad F_{05} = A_\theta F_{04}, \quad F_{07} = A_z F_{04}, \tag{4.19}$$

$$y \to \infty: \quad F_{01}, F_{03}, F_{05}, F_{07} \to 0. \tag{4.20}$$

The right-hand side of (4.18) is associated with the non-parallel effect; the vector $\boldsymbol{G} = \boldsymbol{H}_1\boldsymbol{F}_0$ is given in the Appendix. The problem (4.18)–(4.20) has a non-trivial

solution if its right-hand side is orthogonal to the eigenvector $\xi(x_1, y, \alpha)$of the adjoint problem

$$\left(\frac{\partial}{\partial y} + \boldsymbol{H}_0^T\right)\bar{\boldsymbol{\xi}} = 0, \tag{4.21}$$

$$y = 0: \quad \bar{\xi}_2 = \bar{\xi}_6 = \bar{\xi}_8 = 0, \quad \bar{\xi}_4 + A_x\bar{\xi}_1 + A_y\bar{\xi}_3 + A_\theta\bar{\xi}_5 + A_z\bar{\xi}_7 = 0, \tag{4.22}$$

$$y \to \infty: \quad \bar{\xi}_2, \bar{\xi}_4, \bar{\xi}_6, \bar{\xi}_8 \to 0, \tag{4.23}$$

where the upper bar denotes a complex conjugate value. The orthogonality condition leads to the ordinary differential equation for the amplitude function $c(x_1)$

$$\left\langle \boldsymbol{\xi}, \frac{\partial \boldsymbol{H}_0}{\partial \alpha}\boldsymbol{\zeta} \right\rangle \frac{\mathrm{d}c}{\mathrm{d}x_1} = \left[-\left\langle \boldsymbol{\xi}, \frac{\partial \boldsymbol{H}_0}{\partial \alpha}\frac{\partial \boldsymbol{\zeta}}{\partial x_1} \right\rangle - \mathrm{i}\langle \boldsymbol{\xi}, \boldsymbol{H}_1\boldsymbol{\zeta} \rangle \right] c, \tag{4.24}$$

where the scalar product is defined as

$$\langle \boldsymbol{f}, \boldsymbol{g} \rangle = \int_0^\infty \sum_{j=1}^{8} \bar{f}_j g_j \mathrm{d}y. \tag{4.25}$$

Substituting the solution of (4.24) into (4.17) and (4.13), we express the amplitude vector in the form

$$\boldsymbol{F} = [c_0\boldsymbol{\zeta}(x_1, y) + O(\varepsilon)]\exp\left(\mathrm{i}\varepsilon^{-1}\int [\alpha(x_1) + \varepsilon W(x_1) + O(\varepsilon^2)]\mathrm{d}x_1\right), \tag{4.26}$$

$$W(x_1) = \frac{\mathrm{i}\left\langle \boldsymbol{\xi}, \frac{\partial \boldsymbol{H}_0}{\partial \alpha}\frac{\partial \boldsymbol{\zeta}}{\partial x_1} \right\rangle - \langle \boldsymbol{\xi}, \boldsymbol{H}_1\boldsymbol{\zeta} \rangle}{\left\langle \boldsymbol{\xi}, \frac{\partial \boldsymbol{H}_0}{\partial \alpha}\boldsymbol{\zeta} \right\rangle}, \tag{4.27}$$

where c_0 is constant. The amplification rate of any physical quantity can be calculated using (4.26) and (4.27). For example, the x-component of mass flow disturbance is

$$Q(x_1, y) = [c_0 q(x_1, y) + O(\varepsilon)]\exp\left(\mathrm{i}\varepsilon^{-1}\int [\alpha(x_1) + \varepsilon W(x_1) + O(\varepsilon^2)]\mathrm{d}x_1\right), \tag{4.28}$$

$$q = [\zeta_1 + (\gamma M_e^2\zeta_4 - \zeta_5/T)U]/T. \tag{4.29}$$

The disturbance growth rate is a logarithmic derivative of (4.28), which is expressed in the form

$$\sigma_\alpha(x_1, y) = -\mathrm{Im}\,\alpha + \varepsilon\left(\frac{\partial \ln|q(x_1, y)|}{\partial x_1} - \mathrm{Im}\,W\right) + O(\varepsilon^2). \tag{4.30}$$

Because of the non-parallel effect, the growth rate depends on the vertical coordinate y. According to the experimental measurements, $\sigma_\alpha(x_1, y)$ is calculated at $y = y_m$ relevant to the maximum of mass-flow disturbance in the boundary layer. This maximum lies in the critical layer, where the mean-flow velocity is close to the phase velocity, $U(y) = c$.

The zeroth-order and first-order approximations of σ_α were validated by comparison with the experimental data of Kendall (1967) and the calculations of Chang *et al.* (1991) performed in the framework of linear parabolized stability equations (PSE). Figure 9 shows the first-mode growth rate as a function of the non-dimensional frequency, $F = \omega^* v_e^*/U_e^{*2}$, for the boundary layer on a flat plate at the Mach number $M_e = 2.2$ and the Reynolds number $R = \sqrt{U_e^* L^*/v_e^*} = 1000$. The wave angle is $\psi = \arctan(\beta/\alpha_r) = 60^\circ$. This approximately corresponds to the most unstable waves.

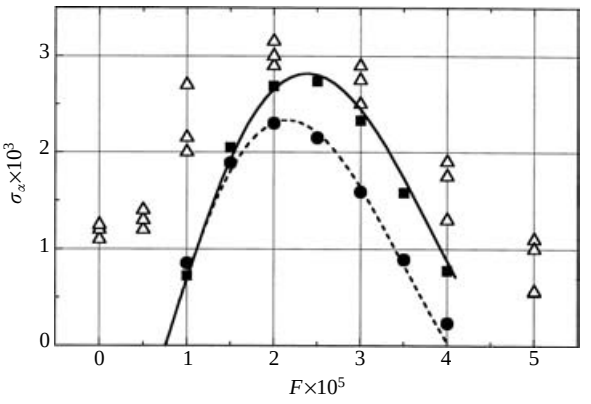

FIGURE 9. The first-mode growth rate as a function of frequency; boundary layer on a flat plate at $M_e = 2.2$, $R = 1000$, the wave angle $\psi = \arctan(\beta/\alpha_r) = 60°$: △, experiment of Kendall (1967); ---, parallel theory (present); ●, parallel theory, Chang *et al.* (1991); —, non-parallel theory (present); ■, non-parallel PSE, Chang *et al.* (1991).

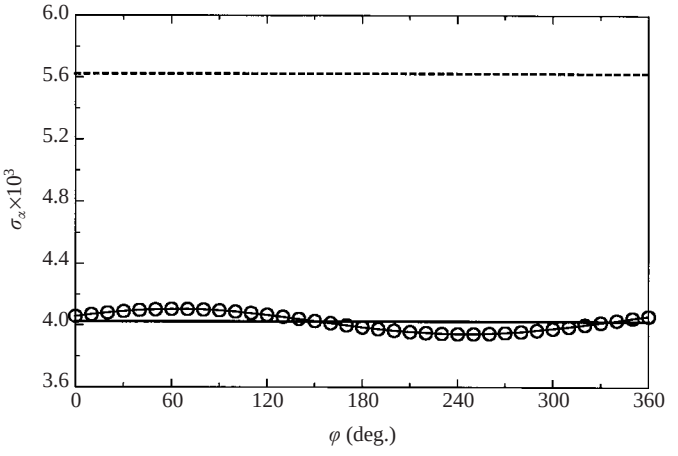

FIGURE 10. Effect of longitudinal admittance on the second-mode stability: $F = 1.2385\times10^{-4}$, $R = 2095$; ---, solid wall; —, $A_y = -1$, $A_x = 0$; ○, $A_y = -1$, $A_x = \exp(i\varphi\,\pi/180)$.

The results are in good agreement with the linear PSE calculations, thereby confirming the aforementioned model.

4.3. *Admittance of porous layer and boundary conditions*

Fedorov & Malmuth (2001) showed that thermal admittance produces a negligible effect on boundary-layer stability. This finding allows us to use the boundary condition $\theta = 0$ at y $= 0$. To estimate effects of the admittance components A_x and A_z, associated with non-zero perturbations of the velocity components u, w on the porous surface, we conducted stability calculations in a wide range of A_x and A_z. This parametric study indicates that the second-mode growth rate weakly depends on A_x and A_z. As an example, figure 10 shows the growth-rate distribution $\sigma_\alpha(\varphi)$ for a two-dimensional disturbance of non-dimensional frequency $F \equiv \omega^* l^*/U_e^* = 1.2385\times10^{-4}$ for a Reynolds number $R \equiv U_e^* l^*/\nu_e^* = 2.095\times10^3$. This case corresponds to the

disturbance of the frequency $f = 250\,\mathrm{kHz}$ at $x^* = 283.2\,\mathrm{mm}$. The calculations were conducted at normal admittance $A_y = -1.0$, transverse admittance $A_z = 0$ and longitudinal admittance $A_x = \exp(\mathrm{i}\varphi\pi/180)$ with φ being measured in degrees. The longitudinal admittance effect is small compared to the normal admittance effect. This feature is due to instability of the hypersonic boundary layer being predominantly governed by an inviscid process. For the limit $R \to \infty$, the system of stability equations is reduced to the two equations coupling the vertical velocity disturbance v and the pressure disturbance p (Mack 1984). Since the other components u, w and θ are passive, their interference with the porous layer weakly affects the disturbance growth rate. Moreover, the felt-metal fibres lie predominantly in the planes, which are orthogonal to the y-axis (see figure 1). Because of this anisotropy, disturbances weakly penetrate in the x- and z-directions compared with the y-direction, i.e. $|A_x| \sim |A_z| \ll |A_y|$. Summarizing, we approximate the boundary conditions on the felt-metal coating as

$$y = 0: \quad u = w = \theta = 0, \quad v = A_y p, \tag{4.31}$$

that is equivalent to the assumption that $A_x = A_z = A_\theta = 0$.

Fedorov & Malmuth (2001) showed that the porous-layer admittance A_y is expressed in the form

$$A_y = \frac{\phi}{Z_0}\tanh(\Lambda h), \tag{4.32}$$

where ϕ is porosity, $h = h^*/l^*$ is the porous-layer thickness, Z_0 and Λ are the characteristic impedance and propagation constant of a porous media, respectively. In the case of cylindrical holes perpendicular to the surface, the characteristic impedance and propagation constant are expressed as a function of the series impedance and the shunt admittance for the tube element of unit length using the transmission line formalism (Daniels 1950; Benade 1968). The same analytical solution can be obtained in terms of the complex dynamic density $\tilde{\rho}$ and the complex dynamic compressibility $\tilde{C}$ (see, for example, Johnson, Koplik & Dashen 1987). Hereafter, we use the latter approach, which is more convenient for analysis of acoustic disturbances in randomly porous media. Accordingly, the characteristic impedance and the propagation constants are expressed as

$$Z_0 = -\frac{\sqrt{\tilde{\rho}/\tilde{C}}}{M_e\sqrt{T_w}}, \quad \Lambda = \frac{\mathrm{i}\omega M_e}{\sqrt{T_w}}\sqrt{\tilde{\rho}/\tilde{C}}, \tag{4.33}$$

where $\tilde{\rho} = \rho^*(\omega)/\rho_w^*$ and $\tilde{C} = \gamma P_w^*/K^*(\omega)$; $K^*(\omega)$ is the dynamic bulk modulus; ρ_w^* and P_w^* are mean density and static pressure in the porous layer, respectively.

The problem of disturbance propagation within the porous layer is decoupled from the boundary-layer stability problem. The former can be treated as a problem of acoustic wave propagation in a porous media, which is characterized by the quantities $\tilde{\rho}$ and $\tilde{C}$. Unfortunately, there is no rigorous theory to predict these characteristics for porous materials of random microstructure. Delany & Bazley (1970) gave empirical relations for $\tilde{\rho}$ and $\tilde{C}$ for fibrous absorbent materials. These relations are widely used in various applications such as sound attenuation in ducts, room acoustics and the transmission loss through walls. Allard & Champoux (1992) modified the correlation of Delany & Bazley (1970) using the theoretical results of Johnson *et al.* (1987). They

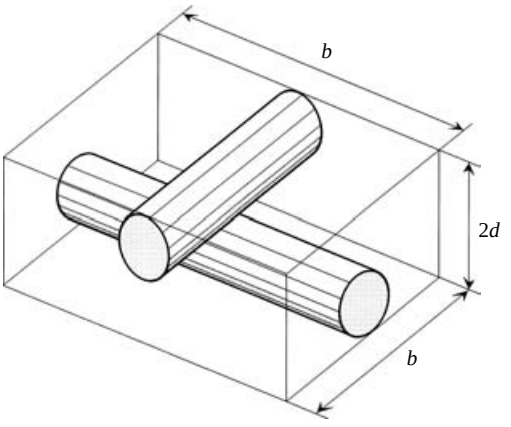

FIGURE 11. An elementary cell of the felt-metal microstructure; $b \times b \times 2d$ parallelepiped including two adjoining sections of fibres with diameter d and mutually orthogonal axes.

derived the semi-empirical relations

$$\tilde{\rho} = a_\infty \left[1 + \frac{g(\lambda_1)}{\lambda_1}\right], \quad \tilde{C} = \gamma - \frac{\gamma - 1}{1 + g(\lambda_2)/\lambda_2}, \tag{4.34}$$

$$g(\lambda) = \sqrt{1 + \frac{4 a_\infty \mu^* \lambda}{\sigma^* \phi r_p^{*2}}}, \tag{4.35}$$

$$\lambda_1 = \mathrm{i} a_\infty \rho_w^* \omega^* / (\phi \sigma^*), \quad \lambda_2 = 4\mathrm{Pr}\lambda_1. \tag{4.36}$$

Here, σ^* is the flow resistivity determined from the equation

$$\Delta P^* = -\sigma^* \Delta Z^* \bar{W}^*, \tag{4.37}$$

which couples the steady pressure drop ΔP^* of viscous flow with the mean flow velocity $\bar{W}^*$ through the porous layer of thickness ΔZ^*. The parameter a_∞ is the tortuosity, which is equivalent to the structure form factor k_s of Zwikker & Kosten (1949) or to the parameter q^2 of Attenborough (1987). It is coupled with the dynamic density $\tilde{\rho}(\omega)$ as $a_\infty = \lim_{\omega \to 0} \tilde{\rho}(\omega)$. The characteristic pore size is defined as

$$r_p^* = \frac{2 \int_V |\boldsymbol{W}^*(\boldsymbol{r}^*)|^2 \, \mathrm{d}V^*}{\int_S |\boldsymbol{W}^*(\boldsymbol{r}_S^*)|^2 \, \mathrm{d}S}. \tag{4.38}$$

The integral in the numerator is evaluated over the pore volume, and $W^*(\boldsymbol{r}^*)$ is the velocity vector of inviscid fluid within the pore; $\boldsymbol{r}^*$ is the radius vector of the point inside the pore volume for which the fluid-velocity vector is defined. The integral in the denominator is taken over the pore surface, and $\boldsymbol{W}^*(\boldsymbol{r}_s^*)$ is the fluid velocity vector on the pore surface. For isotropic porous materials, Allard & Champoux (1992) showed that $r_p^* = s_h \sqrt{8 \mu^* a_\infty / \sigma^* \phi}$, where s_h is the dimensionless shape factor. However, this relation seems not to be valid for the felt-metal, which is highly anisotropic. To resolve this difficulty, we note that the shape factor is $s_h \approx 1$ in the case of cylindrical pores (not necessarily circular), if the fluid velocity is constant. Accordingly, the characteristic pore size r_p^* can be treated as a hydraulic radius, i.e. it is a ratio of the doubled cross-sectional area to the cross-sectional perimeter. To

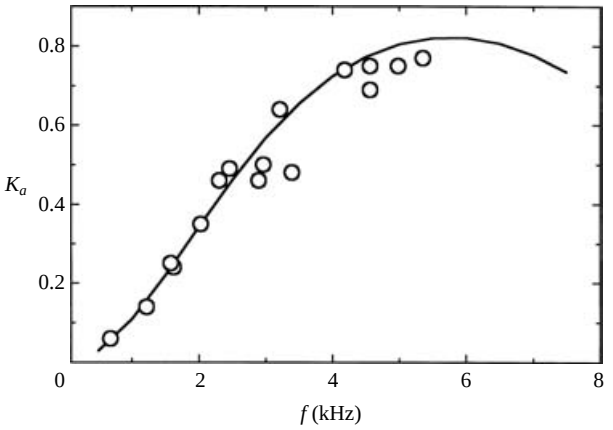

FIGURE 12. The absorption coefficient K_a versus the sound frequency f at the ambient pressure; —, correlation (4.34)–(4.36); ○, laboratory measurements.

estimate r_p^*, we consider an elementary cell (see figure 11) simulating topology of the felt-metal microstructure. The cell is assumed to have the same average statistical properties as the actual porous layer. Accordingly, the characteristic pore size r_p^* and the porosity ϕ are expressed in terms of the fibre diameter d^* and the cell size b^* as

$$r_p^* = 4b^*/(1 + \pi d^*/4b^*), \quad \phi = 1 - \pi d^*/4b^*. \tag{4.39}$$

Using (4.39), we represent r_p^* as a function of the quantities ϕ and d^*, which can be measured experimentally,

$$r_p^* = \frac{\pi d^*}{2(1-\phi)(2-\phi)}. \tag{4.40}$$

Using the method of acoustic standing waves S. Mironov (ITAM) performed laboratory measurements of the felt-metal energy absorption coefficient $K_a = 1 - |R_{ref}|^2$ (where R_{ref} is the reflection coefficient for plane acoustic waves of normal incidence) and coordinates of nodes for standing waves in the resonance tube. The measurements were conducted in the frequency band 1–6 kHz, for which the non-dimensional arguments $\lambda_{1,2}$ of the correlation (4.34)–(4.36) correspond to the wind-tunnel conditions. The best fit of the experimental data gives the felt-metal flow resistivity $\sigma^* = (1.66 \pm 0.21) \times 10^5\,\mathrm{kg\,(m^3\,s^{-1})}$ assuming that the tortuosity $a_\infty = 1$ and the porosity $\phi = 0.75$. With these parameters the relations (4.34)–(4.36) have been used for stability calculations discussed in § 5. Note that 12.6% uncertainty of σ^* is due to a relatively large scatter of the absorption coefficient measurements shown in figure 12 along with the prediction based on (4.34)–(4.36). However, stability calculations of § 5 show that this uncertainty weakly affects the second mode amplification (see figure 16).

Under wind-tunnel conditions, the flow density is relatively small (~1% of the normal density). Because the characteristic pore diameter is also small, rarefied gas effects need to be evaluated. Our estimates show that the mean free path in the porous layer is $\lambda_{mfp}^* \sim 10\,\mu\mathrm{m}$. Using the pore diameter $2r_p^*$ as a characteristic length scale we obtain the Knudsen number $Kn = \lambda_{mfp}^*/2r_p^* \sim 3 \times 10^{-2}$, i.e. the Knudsen-layer thickness is only a few per cent of the pore diameter, and rarefaction effects can be neglected.

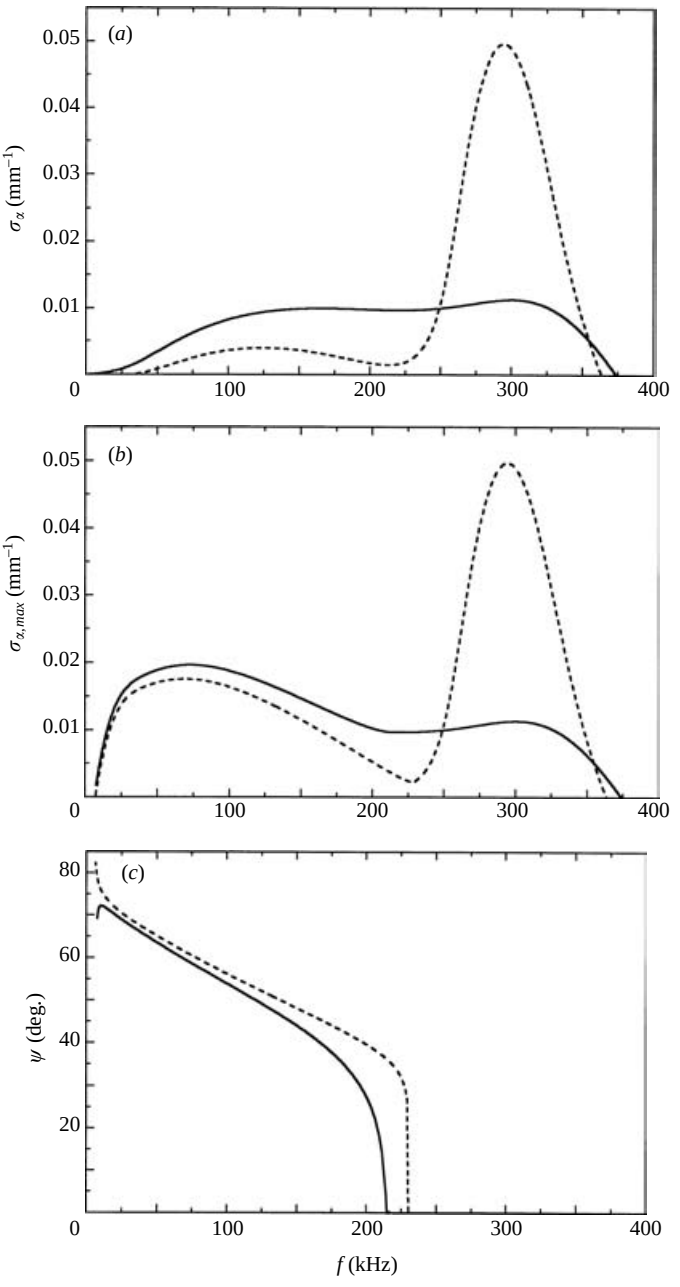

FIGURE 13. (*a*) Growth rate of two-dimensional disturbances *vs.* frequency at $x = 200.1$ mm ($R = 1761.2$); locally parallel approximation. (*b*) Maximum growth rate of three-dimensional disturbances *vs.* frequency at $x = 200.1$ mm ($R = 1761.2$); locally parallel approximation. (*c*) The wave angle $\psi = \arctan(\beta/\alpha_r)$ of the most unstable three-dimensional waves *vs.* frequency at $x = 200.1$ mm ($R = 1761.2$); locally parallel approximation. —, porous wall; ---, solid wall.

5. Stability calculations and comparison with experiment

The first series of stability calculations has been conducted in the local parallel approximation using the system of equations (4.14)–(4.16). Figure 13(*a*) shows the

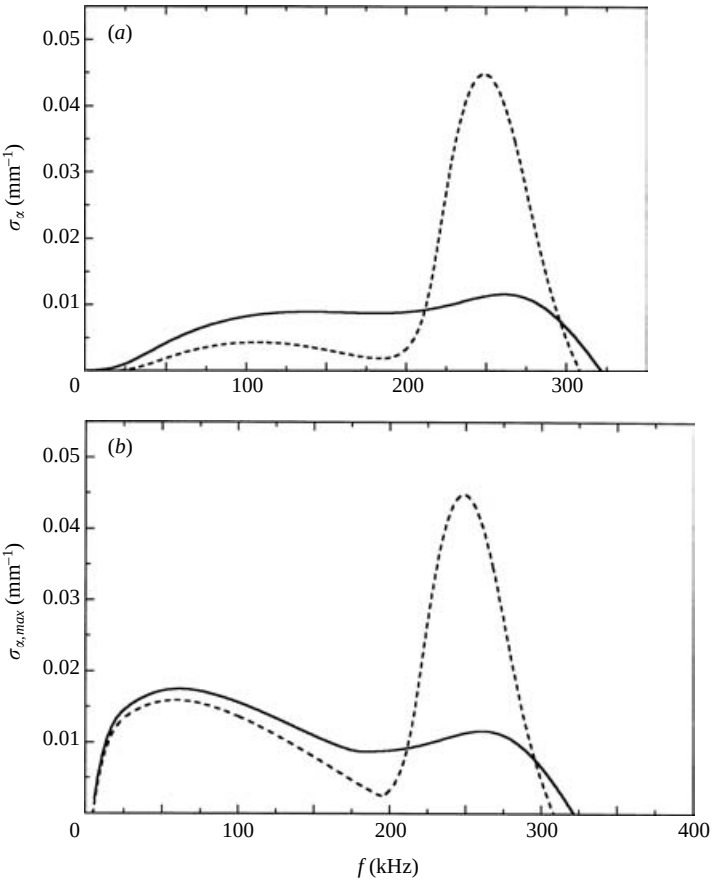

FIGURE 14. Growth rate of two-dimensional disturbances *vs.* frequency at $x = 283.2$ mm ($R = 2095$); locally parallel approximation. Maximum growth rate of three-dimensional disturbances *vs.* frequency at $x = 283.2$ mm ($R = 2095$); locally parallel approximation. ---, solid wall; —, porous wall.

growth rate, $\sigma_\alpha^* = -\mathrm{Im}\,\alpha^*$, of two-dimensional disturbances ($\beta = 0$) as a function of the disturbance frequency f at the streamwise coordinate $x^* = 200.1$ mm. The porous coating strongly stabilizes the second mode relevant to the high-frequency band, $225 < f < 375$ kHz; whereas the first mode associated with low frequencies, $f <$ 225 kHz, is marginally destabilized. Figure 13(*b*) shows similar trends for the maximum growth rate, $\sigma_{\alpha,max}^* = \max[\sigma_\alpha^*(\beta)]$, of three-dimensional disturbances. Figure 13(*c*) shows the wave angle, $\psi = \arctan(\beta/\alpha_r)$, of the most unstable waves. The low-frequency disturbances of maximum amplification are oblique waves relevant to the first mode. In the high-frequency band, the most unstable disturbances are two-dimensional waves (with $\psi = 0$) of the second mode. Similar trends are observed in the case of $x^* = 283.2$ mm shown in figure 14. These results are in qualitative agreement with the experimental data for 'natural' disturbances discussed in § 3.

Figure 15 compares theoretical amplification curves with experimental data for the two-dimensional component of an artificially excited wave packet of frequency $f = 280$ kHz. (See curves (i) and (ii) in figure 7.) In these calculations, the initial amplitudes are adjusted to experimental data at the first data point. For the solid-wall case, the theoretical growth rate is essentially larger than the experimental one,

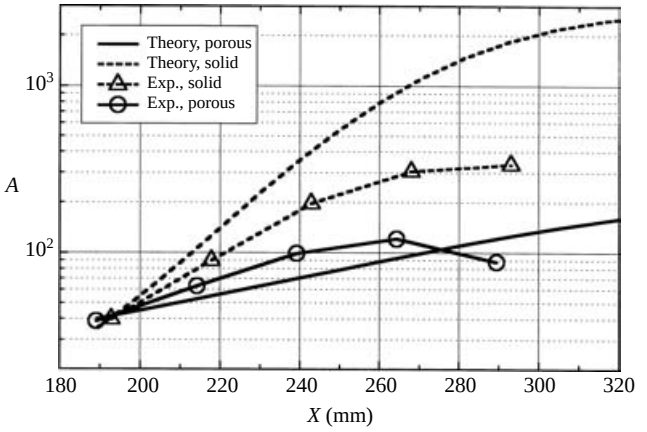

FIGURE 15. Amplification of the two-dimensional component for the artificially excited wave packet of frequency $f = 280\,\mathrm{kHz}$; locally parallel theory versus experiment.

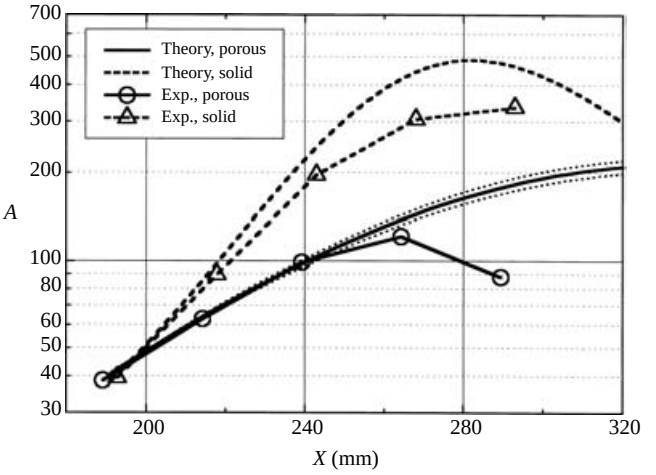

FIGURE 16. Amplification of the two-dimensional component for the artificially excited wave packet of frequency $f = 280\,\mathrm{kHz}$; non-parallel theory versus experiment; —, the felt-metal flow resistivity $\sigma^* = 1.66 \times 10^5\,\mathrm{kg\,m^{-3}\,s^{-1}}, \cdots, \sigma^* = (1.66 \pm 0.21) \times 10^5\,\mathrm{kg\,m^{-3}\,s^{-1}}$.

i.e. the locally parallel approximation gives only qualitative agreement with stability measurements.

To perform a more accurate comparison, we accounted for the non-parallel effect using the first-order approximation, (4.30). According to experimental measurements, the disturbance growth rate $\sigma_\alpha^*(x_1, y)$ was calculated at the vertical coordinate, $y = y_m$, relevant to the maximum of mass-flow pulsations. Figure 16 shows that with this correction, theoretical growth rates (slopes of the amplification curves) are remarkably close to experimental data in the region $190 < x < 260\,\mathrm{mm}$, especially for the porous surface. The dotted lines indicate that an approximately 12% uncertainty in the laboratory measurements of the felt-metal resistivity σ^* leads to much smaller changes of the amplification curve.

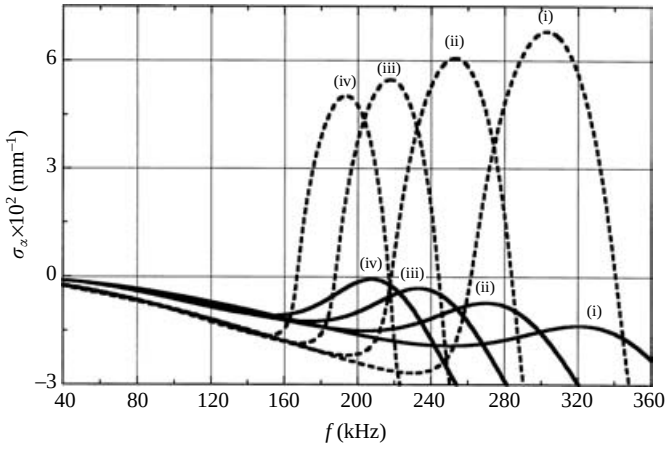

FIGURE 17. Growth rate of two-dimensional disturbances as a function of frequency f at various x, $T_w = 2T_e$, $Re_1 = 10^7\,\mathrm{m}^{-1}$; locally parallel approximation; (i) $x^* = 206.35$ mm, (ii) $x^* = 298.72$ mm, (iii) $x^* = 406.05$ mm, (iv) $x^* = 515.79$ mm. ---, solid wall; —, porous wall.

Finally, we discuss a combination of the UAC and wall cooling effects on the boundary-layer disturbances. We consider the boundary layer at local Mach number $M_e = 5.3$, wall temperature $T_w^* = 2T_e^*$ ($T_w/T_{ad} \approx 0.35$) and the local unit Reynolds number $Re_{1e} = 10^7\,\mathrm{m}^{-1}$. Stability calculations for various β show that, in contrast to the adiabatic wall case, the most unstable waves are two-dimensional for both low and high frequencies. Seemingly, wall cooling leads to a stronger stabilization of the first-mode oblique waves than the two-dimensional waves. Figure 17 shows the growth rates of two-dimensional disturbances as functions of the frequency f at various x^* stations. The porous coating leads to a dramatic reduction of σ_α for high frequencies associated with the second mode instability. In the low-frequency band of the first mode, the coating causes a marginal increase of σ_α. However, the wall cooling leads to such a strong stabilization of the first mode that the low-frequency waves are stable everywhere. This example demonstrates that the porous coating on a cold wall causes a massive damping of unstable disturbances. Note that for actual hypersonic vehicles, the wall temperature ratio is small (less than 0.2) enough to eliminate the first-mode instability. With the help of a passive porous coating, it is feasible to diminish the second-mode instability and significantly increase the laminar run on hypersonic vehicle surfaces.

6. Conclusions

Experimental and theoretical studies of hypersonic boundary-layer stability were performed for ultrasonically absorptive coatings (UAC) of random microstructure. Such structures typify practical TPS materials. Stability of natural disturbances and artificially excited wave packets in the boundary layer on solid and porous surfaces of a sharp cone were measured in the ITAM Mach 6 wind tunnel. These results were compared with stability analyses that included theoretical simulations of the UAC characteristics.

The experiments were conducted on a 7° half-angle sharp cone, one half of which is solid and the other covered by a thin porous coating of random microstructure. Hot-wire measurements showed that boundary layers on solid and porous surfaces

are laminar. The mean flow profiles are similar in both cases and agree with the self-similar solution of the boundary-layer equations. The hot-wire measurements of 'natural' disturbances showed that the disturbance spectra on the solid surface are typical for hypersonic boundary layers, with the second mode being dominant. On the porous surface, the second mode is so strongly suppressed that it is not observable in the measurement region, while the first mode becomes unstable. To investigate the second mode stabilization effect, artificial wave packets were generated in the boundary layer at a frequency relevant to the second mode instability. Two-dimensional waves of the wave packets were dominant and unstable on the solid surface. Additionally, the porous coating reduced the second-mode growth rate.

A linear stability problem was formulated for the boundary layer on a sharp cone with and without a porous coating. A major effect of the coating is associated with porous-layer admittance to vertical velocity disturbances. Non-zero perturbations of the longitudinal and transverse velocity components on the porous surface weakly affect the second-mode instability and can be neglected. With this approximation, the porous coating admittance was determined using the semi-empirical relations of Allard & Champoux (1992) and laboratory measurements of the felt-metal characteristics.

Stability calculations for two- and three-dimensional disturbances showed that the felt-metal coating strongly stabilizes the second mode relevant to the high-frequency band and marginally destabilizes the first mode of relatively low frequencies. These results are in qualitative agreement with experimental data for natural disturbances.

Comparison of the theoretical amplification curves with the experimental data for a two-dimensional component of an artificially excited wave packet showed that the theoretical growth rate is larger than the experimental one. The locally parallel approximation of the stability problem gives only qualitative agreement with the stability measurements. The mean-flow non-parallel effect, associated with the downstream growth of the boundary layer, was incorporated into the stability analysis. With this correction, theoretical growth rates are remarkably close to experimental data (especially for the porous wall case), which confirms the theoretical model.

Stability calculations for the cooled-wall case indicated that wall cooling leads to a strong stabilization of the first mode, while the second mode is effectively suppressed by the porous coating. For actual hypersonic vehicles, the wall temperature ratio is small (less than 0.2), which eliminates the first-mode instability. Using a passive porous coating, it is feasible to diminish the second-mode instability and significantly increase the laminar run on actual hypersonic vehicle surfaces with predominantly two-dimensional boundary layers.

The authors acknowledge Dr Adam Rasheed who kindly provided the information on the felt metals. We also thank Dr Sergei Mironov for the benchmark measurements of the felt-metal characteristics and Dr Vitaly Kozlov for his help in analysing the benchmark data and evaluating the acoustic properties of the felt-metal coating.

Portions of this work were sponsored by Boeing and the Air Force Office of Scientific Research Contract No. F49620-99-0005. The US government is authorized to reproduce and distribute reprints for government purposes, notwithstanding any copyright notation thereon. The views and conclusions herein are those of the authors and should not be interpreted as necessarily representing the official policies or endorsements, either expressed or implied, of the Air Force Office of Scientific Research or the US government.

Appendix

$\mathrm{D} = \mathrm{d}/\mathrm{d}y$, $\mu' = \mathrm{d}\mu/\mathrm{d}T$, $m = \frac{2}{3}(e-1)$, $r = (e+2)$, where $e = 1.2$ corresponds to the ratio of the second viscosity to the first viscosity $\mu_2/\mu = \frac{2}{3}e = 0.8$; $\chi = [(R/\mu) + \mathrm{i}r\gamma M_e^2(\alpha U - \omega)]^{-1}$. Non-zero elements of the matrix $\boldsymbol{H}_0$ in (4.14) are

$$H_{12} = H_{56} = H_{78} = 1;$$

$$H_{21} = \alpha^2 + \beta^2 + \mathrm{i}(\alpha U - \omega)\frac{R}{\mu T}, \quad H_{22} = -\frac{\mathrm{D}\mu}{\mu},$$

$$H_{23} = -\mathrm{i}\alpha\left[(m+1)\frac{\mathrm{D}T}{T} + \frac{\mathrm{D}\mu}{\mu}\right] + \frac{R\mathrm{D}U}{\mu T},$$

$$H_{24} = \mathrm{i}\frac{\alpha R}{\mu} - (m+1)\gamma M_e^2\alpha(\alpha U - \omega), \quad H_{25} = (m+1)\frac{\alpha}{T}(\alpha U - \omega) - \frac{\mathrm{D}(\mu'\mathrm{D}U)}{\mu},$$

$$H_{26} = -\frac{\mu'\mathrm{D}U}{\mu};$$

$$H_{31} = -\mathrm{i}\alpha, \quad H_{33} = \frac{\mathrm{D}T}{T}, \quad H_{34} = -\mathrm{i}\gamma M_e^2(\alpha U - \omega), \quad H_{35} = \frac{\mathrm{i}}{T}(\alpha U - \omega), \quad H_{37} = -\mathrm{i}\beta;$$

$$H_{41} = -\mathrm{i}\alpha\chi\left(r\frac{\mathrm{D}T}{T} + 2\frac{\mathrm{D}\mu}{\mu}\right), \quad H_{42} = -\mathrm{i}\alpha\chi,$$

$$H_{43} = \chi\left[-\alpha^2 - \beta^2 + r\frac{\mathrm{D}\mu\mathrm{D}T}{\mu T} + r\frac{\mathrm{D}^2T}{T} - \mathrm{i}\frac{R}{\mu T}(\alpha U - \omega)\right],$$

$$H_{44} = -\mathrm{i}\chi r\gamma M_e^2\left[\alpha\mathrm{D}U + \left(\frac{\mathrm{D}T}{T} + \frac{\mathrm{D}\mu}{\mu}\right)(\alpha U - \omega)\right],$$

$$H_{45} = \mathrm{i}\chi\left[r\alpha\frac{\mathrm{D}U}{T} + \alpha\frac{\mu'\mathrm{D}U}{\mu} + r\frac{\mathrm{D}\mu}{\mu T}(\alpha U - \omega)\right],$$

$$H_{46} = \mathrm{i}\chi\frac{r}{T}(\alpha U - \omega), \quad H_{47} = -\mathrm{i}\beta\chi\left(r\frac{\mathrm{D}T}{T} + 2\frac{\mathrm{D}\mu}{\mu}\right), \quad H_{48} = -\mathrm{i}\beta\chi;$$

$$H_{62} = -2\,\mathrm{Pr}(\gamma-1)M_e^2\mathrm{D}U, \quad H_{63} = R\,\mathrm{Pr}\frac{\mathrm{D}T}{\mu T} - 2\mathrm{i}\alpha(\gamma-1)M_e^2\mathrm{Pr}\,\mathrm{D}U,$$

$$H_{64} = -\mathrm{i}R\,\mathrm{Pr}\frac{(\gamma-1)M_e^2}{\mu}(\alpha U - \omega),$$

$$H_{65} = \alpha^2 + \beta^2 + \mathrm{i}R\,\mathrm{Pr}\frac{(\alpha U - \omega)}{\mu T} - (\gamma-1)M_e^2\,\mathrm{Pr}\frac{\mu'(\mathrm{D}U)^2}{\mu} - \frac{\mathrm{D}^2\mu}{\mu}, \quad H_{66} = -2\frac{\mathrm{D}\mu}{\mu};$$

$$H_{83} = -\mathrm{i}\beta\left[(m+1)\frac{\mathrm{D}T}{T} + \frac{\mathrm{D}\mu}{\mu}\right], \quad H_{84} = \mathrm{i}\frac{\beta R}{\mu} - (m+1)\gamma M_e^2\beta(\alpha U - \omega),$$

$$H_{85} = (m+1)\frac{\beta}{T}(\alpha U - \omega), \quad H_{87} = \alpha^2 + \beta^2 + \mathrm{i}(\alpha U - \omega)\frac{R}{\mu T}, \quad H_{88} = -\frac{\mathrm{D}\mu}{\mu}.$$

The vector $\boldsymbol{G} = \boldsymbol{H}_1\boldsymbol{F}_0$ in (4.18) is expressed as

$$\boldsymbol{F}_0 \equiv (f_1, f_2, \ldots, f_8)^T,$$

$$G_1 = G_5 = G_7 = 0,$$

$$G_2 = \frac{R}{\mu}\left[\frac{f_1}{T}\frac{\partial U}{\partial x_1} + \frac{V_0}{T}\frac{\partial f_1}{\partial y} + \left(\frac{\gamma M_e^2 f_4}{T} - \frac{f_5}{T^2}\right)\left(U\frac{\partial U}{\partial x_1} + V_0\frac{\partial U}{\partial y}\right)\right],$$

$$G_3 = \frac{f_1}{T}\frac{\partial T}{\partial x_1} + \gamma M_e^2 f_4 \frac{U}{T}\frac{\partial T}{\partial x_1} - f_5 \frac{2U}{T^2}\frac{\partial T}{\partial x_1} - \left(\gamma M_e^2 f_4 - \frac{f_5}{T}\right)\left(\frac{\partial U}{\partial x_1} + \frac{\partial V_0}{\partial y}\right)$$
$$- \gamma M_e^2 V_0 \left[\left(\frac{\partial f_4}{\partial y} - \frac{f_4}{T}\frac{\partial T}{\partial y}\right) - \frac{1}{T}\frac{\partial f_5}{\partial y} + \frac{2f_5}{T^2}\frac{\partial T}{\partial y}\right],$$

$$G_4 = -\frac{1}{T}\left(V_0 \frac{\partial f_3}{\partial y} + f_3 \frac{\partial V_0}{\partial y}\right),$$

$$G_6 = -\frac{R\mathrm{Pr}}{\mu}\left[-\frac{V_0}{T}\frac{\partial f_5}{\partial y} - \left(\frac{\gamma M_e^2 f_4}{T} - \frac{f_5}{T^2}\right)\left(U\frac{\partial T}{\partial x_1} + V_0 \frac{\partial T}{\partial y}\right)\right.$$
$$\left. + (\gamma - 1) M_e^2 \left(V_0 \frac{\partial f_4}{\partial y} - \frac{f_1}{T}\frac{\partial T}{\partial x_1}\right)\right],$$

$$G_8 = \frac{R}{\mu}\frac{V_0}{T}\frac{\partial f_7}{\partial y}.$$

REFERENCES

Allard, J.-F. & Champoux, Y. 1992 Empirical equations for sound propagation in rigid frame porous materials. *J. Acoust. Soc. Am.* **91**, 3346–3353.

Attenborough, K. 1987 On the acoustic slow wave in air-filled granular media. *J. Acoust. Soc. Am.* **81**, 93–102.

Benade, A. H. 1968 On the propagation of sound waves in a cylindrical conduit. *J. Acoust. Soc. Am.* **44**, 616–623.

Carpenter, P. W. & Porter, L. J. 2001 Effects of passive porous walls on boundary-layer stability. *AIAA J.* **39**, 597–604.

Chang, C.-L., Malik, M. R., Erlebacher, G. & Hussaini, M. Y. 1991 Compressible stability of growing boundary layers using parabolized stability equations. *AIAA Paper* 91-1636.

Daniels, F. B. 1950 On the propagation of sound waves in a cylindrical conduit. *J. Acoust. Soc. Am.* **22**, 563–564.

Delany, M. A. & Bazley, E. N. 1970 Acoustic properties of fibrous absorbent materials. *Appl. Acoust.* **3**, 105–116.

Demetriades, A. 1974 Hypersonic viscous flow over a slender cone. Part III: Laminar instability and transition. *AIAA Paper* 74-535.

El-Hady, N. M. 1980 On the stability of three-dimensional compressible nonparallel boundary layers. *AIAA Paper* 80-1374.

Fedorov, A. V. & Khokhlov, A. P. 2002 Receptivity of hypersonic boundary layer to wall disturbances. *Theor. Comput. Fluid Dyn.* **15**, 231–254.

Fedorov, A. V. & Malmuth, N. D. 2001 Stabilization of hypersonic boundary layers by porous coatings. *AIAA J.* **39**, 605–610.

Gaponov, S. A. 1971 Influence of porous layer on boundary layer stability. *Izv. SO AN SSSR Ser. Tekh. Nauk* **1**, 21–23 (in Russian).

Gaponov, S. A. 1975 Influence of gas compressibility on stability of boundary layer on porous surface at subsonic speeds. *Zh. Prikl. Mekh. i Tekh. Fiz.* **1**, 121–125 (in Russian).

Gaponov, S. A. 1977 Stability of supersonic boundary layer on porous wall with heat conductivity. *Izv. AN SSSR Mekh. Zhid. i Gaza* **1** (in Russian).

Gaponov, S. A. 1980 Effect of nonparallel flow on propagation of disturbances in a supersonic boundary layer. *Izv. AN SSSR Mekh. Zhid. i Gaza* **2**, pp. 26–31 (in Russian).

Gaster, M. 1974 On the effects of boundary-layer growth on the flow stability. *J. Fluid Mech.* **66**, 465–480.

Grigoriev, V. D., Klemenkov, G. P., Omelaev, A. I. & Kharitonov, A. M. 1972 Hypersonic wind tunnel T-326. In *Aerofizicheskie Issledovania* (ed. A. M. Kharitonov), pp. 16–18. Novosibirsk (in Russian).

Gushchin, V. R. & Fedorov, A. V. 1989 Asymptotic analysis of inviscid perturbations in a supersonic boundary layer. *Zh. Prikl. Mekh. i Tekh. Fiz.* **1**, 69–75 (in Russian).

Hayes, W. D. & Probstein, R. F. 1959 *Hypersonic Flow Theory*. Academic.

Johnson, D. L., Koplik, J. & Dashen, R. 1987 Theory of dynamic permeability and tortuosity in fluid saturated porous media. *J. Fluid Mech.* **176**, 379–402.

Kendall, J. M. 1967 Supersonic boundary layer stability experiments. *Proc. of Transition Study Group Meeting*, vol. 2 (ed. W. D. McCauley). Aerospace Corp., San Bernardino, CA.

Kendall, J. M. 1975 Wind tunnel experiments relating to supersonic and hypersonic boundary-layer transition. *AIAA J.* **13**, 290–299.

Kimmel, R., Demetriades, A. & Donaldson, J. 1995 Space–time correlation measurements in a hypersonic transitional boundary layer. *AIAA paper* 95-2292.

Kosinov, A. D., Maslov, A. A. & Shevelkov, S. G. 1990 Experiments on the stability of supersonic laminar boundary layers. *J. Fluid Mech.* **219**, 621–633.

Lecoudis, S. G. 1978 Stability of boundary layers over permeable surfaces. *AIAA Paper* 78-203.

Lysenko, V. I. & Maslov, A. A. 1984 The effect of cooling on supersonic boundary-layer stability. *J. Fluid Mech.* **147**, 38–52.

Mack, L. M. 1984 Boundary-layer stability theory. Special course on stability and transition of laminar flow (ed. R. Michel), *AGARD Rep.* **709**, pp. 3-1–3-81.

Malik, M. R. 1989 Prediction and control of transition in supersonic and hypersonic boundary layers. *AIAA J.* **27**, 1487–1493.

Malik, M. R., Zang, T. A. & Bushnell, D. M. 1990 Boundary layer transition in hypersonic flows. *AIAA Paper* 90-5232.

Malmuth, N. D., Fedorov, A. V., Shalaev, V., Cole, J. & Khokhlov, A. 1998 Problems in high speed flow prediction relevant to control. *AIAA Paper* 98-2695.

Maslov, A. A., Shiplyuk, A. N., Sidorenko, A. A. & Arnal, D. 2001 Leading-edge receptivity of a hypersonic boundary layer on a flat plate. *J. Fluid Mech.* **426**, 73–94.

Padhye, A. R. & Nayfeh, A. H. 1979 Nonparallel stability of three-dimensional flows. *AIAA Paper* 79-1278.

Rasheed, A., Hornung, H. G., Fedorov, A. V. & Malmuth, N. D. 2002 Experiments on passive hypervelocity boundary layer control using an ultrasonically absorptive surface. *AIAA J.* **40**, 481–489.

Reshotko, E. 1969 Stability theory as a guide to the evaluation of transition data. *AIAA J.* **7**, 1086–1091.

Reshotko, E. 1994 Boundary layer instability, transition and control. *AIAA Paper* 94-0001.

Stetson, K. F. & Kimmel, R. G. 1992*a* On hypersonic boundary-layer stability. *AIAA Paper* 92-0737.

Stetson, K. F. & Kimmel, R. G. 1992*b* Example of second-mode instability dominance at a Mach number of 5.2. *AIAA J.* **30**, 2974–2976.

Stetson, K. F., Thompson, E. R., Donaldson, J. C. & Siler, L. G. 1983 Laminar boundary layer stability experiments on a cone at Mach 8. Part 1: Sharp cone. *AIAA Paper* 83-1761.

Tumin, A. M. & Fedorov, A. V. 1982 On the weakly nonparallel effect on characteristics of flow stability. *Uchenye Zapiski TsAGI* **13**(6), 91–96 (in Russian).

Zhigulev, V. N. & Tumin, A. M. 1987 *Onset of Turbulence*. Nauka, Novosibirsk (in Russian).

Zwikker, C. & Kosten, C. W. 1949 *Sound Absorbing Materials*. Elsevier.